Experimental Study of Nonlinear Processes in Edge Turbulence of Toroidal Plasmas

Yoshihiko NAGASHIMA, Katsumichi HOSHINO[1], Kenichi NAGAOKA[2], Kouji SHINOHARA[1],
Akihide FUJISAWA[2], Kazuya UEHARA[1], Yoshinori KUSAMA[1], Katsumi IDA[2],
Yasuo YOSHIMURA[2], Shoichi OKAMURA[2], Keisuke MATSUOKA[2], Akira EJIRI[3],
Yuichi TAKASE[3], Kimitaka ITOH[2], Masatoshi YAGI, Sanae-I. ITOH, JFT-2M group[1]
and CHS group[2]

Research Institute for Applied Mechanics, Kyushu University, Fukuoka 816–8580, Japan
[1]*Japan Atomic Energy Agency, Ibaraki 311–0193, Japan*
[2]*National Institute for Fusion Science, Toki 509–5292, Japan*
[3]*University of Tokyo, Kashiwa 227–8561, Japan*

This paper presents experimental studies of nonlinear processes between meso-scale structures and turbulent fluctuations, by use of bispectral analysis, in the edge region of toroidal plasmas. In ohmically heated plasmas of the JFT-2M tokamak, the drift wave-zonal flow system is investigated by observation of the potential fluctuations. The total bicoherence is composed of two components, i.e., the peak at the geodesic acoustic mode (GAM) frequency and broadband distribution. The biphase is also obtained, which indicates the phase angle of coherent interaction between GAM oscillations and broadband fluctuations. Bispectral functions (e.g., magnitude and phase) give an order-of-estimate agreement for the drift wave-zonal flow systems. Bicoherence analysis is also applied to the edge plasmas of the high-confinement mode (H-mode) of the Compact Helical System (CHS). In the case of CHS plasmas, nonlinear couplings in a system composed of coherent global magneto-hydrodynamic (MHD) oscillations and broadband fluctuations (up to hundreds kHz range) have been observed. Bispectral analysis enhances our understanding of the self-regulation systems of various toroidal plasmas in which strong turbulence and meso-scale structures coexist.

1. Introduction

Much study has been devoted to the understanding of turbulence and turbulent transport in toroidal plasmas. Progress in turbulence theory has revealed essential features of nonlinear interactions between meso-scale structures and strong turbulence [1–4]. Recent progress has highlighted the importance of zonal flows in drift wave turbulence [5, 6]. (Zonal flows are toroidally and azimuthally symmetric band-like shear flows, which are nonlinearly driven by drift wave turbulence and that regulate turbulence and turbulent transport.) The other key example of multiple-scale interactions [7] is the interaction between the magneto-hydrodynamic (MHD) modes and background turbulence. Turbulence-driven resistivity can enhance the growth rate of the resistive MHD instability. In addition to this type of nonlinear effect, the direct coupling of turbulence to the MHD mode is also effective, so that the subcritical excitation of nonlinear instability of the MHD mode has been predicted [8]. Such direct excitation of the MHD mode by drift wave turbulence has also been

confirmed by direct nonlinear simulation [9]. The necessity for the direct experimental observation of nonlinear coupling effects (in zonal flow - drift wave system, the ZF-DW system, as well as in the MHD mode in background turbulence) is widely recognized.

Bispectral analysis is an important tool in quantifying three-wave interactions in experimental data [10, 11]. This analysis has been applied to various plasma experiments [12–20] and has contributed much to the understanding of, e.g., the nonlinear interaction among drift wave turbulence, the Reynolds-stress drive for zonal flows, the onset of the high-confinement mode (H-mode) transition, and so on. In addition, the reality of the zonal flow has been confirmed experimentally [21], and the need for bispectral analysis has increased. Quantitative interpretations of the bispectral data have also been obtained by the progress in the theory's development. For example, an interpretation of bispectral functions has been discussed in Refs. [15, 22]. In a previous article [19], the bispectral analysis of the edge fluctuation data in the JFT-2M tokamak [23] (limiter configuration) has been reported. Coherent modes (CMs) were ob-

served, which were attributed to geodesic acoustic modes (GAMs) [24]. The bicoherence spectrum was obtained for the interaction between the coherent fluctuations and the background fluctuations.

In the present article, we perform bispectral analysis of the edge fluctuation data in ohmically heated discharges in the JFT-2M tokamak. The diverter plasmas are analyzed. Significant bicoherence is measured, allowing the quantitative evaluation of the nonlinear interaction based on the experimental data. The biphase is also measured. It is found that the biphase at the frequency of the coherent fluctuations has a sharp peak over the variation of the frequency of the coupled modes. In contrast, the biphase at the frequency of the background fluctuations shows a wide scatter. The experimental observations of the bispectral functions, the biphase, and the total bicoherence are compared with the theoretical expectations. Compared to the results reported in a previous article [25], the difference of the configuration (from the limiter to the diverter) leads to the difference of the plasma parameters. Thus the real frequency of GAMs or the intensity of the broadband spectrum differs in these two cases. These differences consistently appear in the difference of the bispectra.

We next discuss the bispectral analysis of the edge plasma data in the H-mode discharges of the CHS (Compact Helical System) device. In this case, fluctuations are composed of three elements: (i) the low-frequency coherent MHD mode, (ii) the broadband fluctuations in the range of 10–100 kHz, and (iii) the high-frequency broadband fluctuations at 100–500 kHz. A sharp peak of the bicoherence at the coherent mode frequency, and broad distribution of the bicoherence for broadband fluctuations are observed. The interaction between the coherent mode and broadband fluctuations are studied. The intensity of the nonlinear coupling between them is also discussed. These measurements provide a basis for studying the nonlinear coupling between the MHD mode and background fluctuations.

Thus, this article provides a step forward in the quantitative experimental measurement of the nonlinear interactions of the DW-ZF systems as well as those in the system of the MHD mode and turbulent fluctuations.

This article is organized as follows. In Sec. 2, definition of the bispectral analysis is briefly introduced. In Sec. 3, results from the JFT-2M device are presented. Experimental conditions and the layout of the diagnostics are described first. Next, the experimental results regarding the quadratic spectra are shown. Then, the results of bispectral analysis are given. Interpretation of the data, through comparison with the theoretical results, is discussed at the end of this chapter. In Sec. 4, the results from the CHS device are discussed. The experimental setup, the time evolutions of the discharge waveforms, and the quadratic spectra in the H-mode plasmas are explained. The results of the bispectral analysis are then illustrated. The interpretation of the bicoherence data is finally ex-

plained. Summary and general discussion are included in Sec. 5.

2. Bispectral Analysis

The bispectrum [11] is the third order cumulant spectrum and is defined as,

$$\hat{B}(f_1, f_2) = \langle Y(f_1)Y(f_2)Y^*(f_3 = f_1 \pm f_2) \rangle, \qquad (1)$$

where $Y(f)$ is the Fourier component of the observed time-series $y(t)$, f is the frequency, and $f_3 = f_1 \pm f_2$ is satisfied. This type of bispectrum, composed of the Fourier components of the same time-series, is referred to as the auto-bispectrum. The bispectrum composed of different time-series is referred to as the cross-bispectrum, and is defined as

$$\hat{B}(f_1, f_2) = \langle X(f_1)Y(f_2)Z^*(f_3 = f_1 \pm f_2) \rangle, \qquad (2)$$

where $X(f)$ and $Z(f)$ are the Fourier components of the observed time-series $x(t)$ and $z(t)$, respectively. In this paper, only the results of auto-bispectra are presented. The bispectral analysis can clarify three-wave nonlinear interactions (e.g., Lagrangian nonlinearity or parametric-modulational instabilities). Three-wave interactions occur under the condition that $\mathbf{k}_3 = \mathbf{k}_1 \pm \mathbf{k}_2$ and $f_3 = f_1 \pm f_2$, where $\mathbf{k}_{1, 2, 3}$ and $f_{1, 2, 3}$ are wavenumbers and frequencies of the three waves, respectively.

For investigating the occurrence of three-wave interaction qualitatively, it is convenient to introduce the squared bicoherence. The squared bicoherence is a squared normalized bispectrum, and is defined as

$$\hat{b}^2(f_1, f_2) = \frac{|\hat{B}(f_1, f_2)|^2}{\langle |Y(f_1)Y(f_2)|^2 \rangle \langle |Y(f_3)|^2 \rangle}. \qquad (3)$$

Bicoherence indicates a fractional contribution of three-wave nonlinear couplings to full third Fourier components. In practice, quantitative meanings of the squared bicoherence in plasma turbulence are also presented in a theory paper [22].

The total bicoherence, a summation of the squared bicoherence, is convenient for representing the nonlinear contribution from many modes to a single mode, and is defined as

$$\sum \hat{b}^2 = \sum_{f_3 = f_1 \pm f_2} \hat{b}^2(f_1, f_2). \qquad (4)$$

Thus, the total bicoherence $\sum \hat{b}^2$ is given on a familiar of one frequency f_3.

The phase angle of the three-wave interaction is shown as the biphase. The biphase is the complex phase angle of $\hat{B}(f_1, f_2)$, and is defined as

$$\theta = \tan^{-1} \frac{\text{Im } \hat{B}(f_1, f_2)}{\text{Re } \hat{B}(f_1, f_2)}. \qquad (5)$$

For quantitative tests of the results of bispectral analysis, it is indispensable to obtain bispectral functions that

are sufficiently converged and much larger than the significance level (statistical variance). The significance level of bispectral analysis is reviewed in Refs. [11, 26]. A Fourier component can be expressed by the summation of two terms: one term is nonlinearly driven by other Fourier components, and the other term exists independently or is driven by non-observed components. The former is the relevant part, and the latter term includes the measurement uncertainty as well. (For convenience, the latter term is called "independent fluctuations" in this paper.) The significance level is determined by the squared bicoherence of "independent fluctuations" and has a value of $(1 - \hat{b}^2)/M$, where M is the number of realizations, assuming that the variances of the average auto-power spectra $\langle |Y(f_3)|^2 \rangle$ and cross-power spectra $\langle |Y(f_1)Y(f_2)|^2 \rangle$ are negligibly small. Precise bispectral functions can be obtained in the limit of $M \to \infty$, where the significance level goes to zero and the bispectral functions are "converged". For instance, the total bicoherence $\sum \hat{b}^2$ is obtained for various values of realizations M, and is fitted in a form of $C_1 + (C_2/M)$. The value C_1 is considered to be the converged value. Practically speaking, therefore, it is important to obtain a large number of realizations M in order to improve the signal to noise ratio and to clarify the significant nonlinear couplings. The details of a convergence study in the case of JFT-2M plasmas are reported in a separate article [27].

3. Results from the JFT-2M Tokamak: Observation of Drift Wave-Zonal Flow Systems

In this section, experimental results using the JFT-2M tokamak [23] with the diverter configurations are presented. In the edge region of ohmically heated plasmas and the low-confinement mode plasmas (L-mode), coherent potential fluctuations around GAM frequency have been observed by a reciprocating Langmuir probe [19] and a heavy ion beam probe (HIBP) [28]. The coherent modes (CMs) are inferred as the GAMs. (See Ref. [28] for details of the conclusion that the observed CMs are GAMs.) In both diagnostics, the bicoherence estimators show significant nonlinear coupling between the GAM and the broadband turbulent fluctuations. First, experimental setups are described. Second, the experimental results regarding the quadratic spectra, i.e., the auto-power spectra, poloidal cross-coherence, and poloidal wavenumber derived from cross-phase of floating potential fluctuations are shown. Next, results of the bispectral analysis are described. Interpretation of the data, through comparison with theoretical results, is discussed.

3.1 Experimental setup of the JFT-2M tokamak

The JFT-2M device is a medium-size tokamak device, with a major radius at the plasma center $R_0 = 1.31$ m, mi-
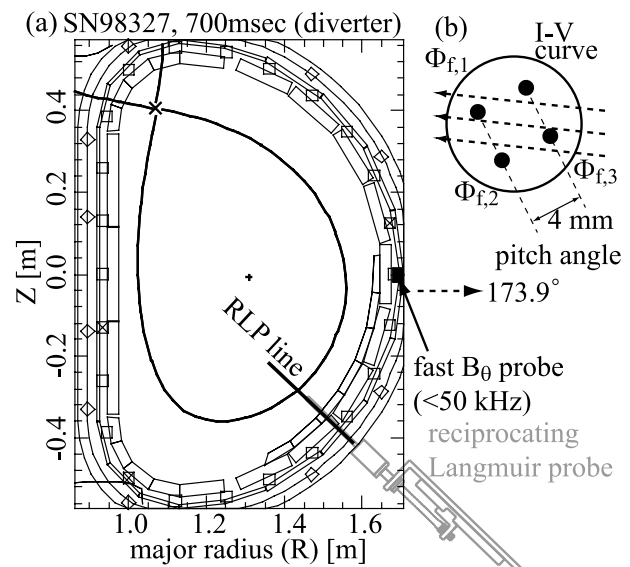

Fig. 1 (a) Magnetic configuration of a diverter plasma and locations of diagnostics on JFT-2M. (b) Head-on view of the reciprocating Langmuir probe (RLP) and magnetic field-lines.

nor radius $a = 0.35$ m, elongation $\kappa \leq 1.7$, and toroidal magnetic field $B_t \leq 2.2$ T. Edge fluctuation measurements were performed using a reciprocating Langmuir probe (RLP) [29]. Figure 1 (a) illustrates the geometry of the plasma and the RLP, together with the outermost magnetic surface of a typical diverter plasma. The RLP head houses four electrodes arranged at four corners of a 4 mm square. The head surface is approximately tangent to the local magnetic flux surface. The square is inclined by 26.5 degrees from the toroidal direction, as shown in Fig. 1 (b), in order to avoid the shadowing effect of one probe on the other along the magnetic field line. Cylindrical electrodes with a diameter of 1 mm and a height of 0.5 mm are made of molybdenum. One electrode is used as a Langmuir probe with a triangular voltage sweep at 1 kHz. The ion saturation current ($I_{i,sat}$) data are obtained over a 500 μs interval during each sweep when the mean positive probe current (ion current) is saturated. The three other electrodes are used for measuring the floating potential (Φ_f). The RLP data have an analog bandwidth up to 100 kHz and are digitized by a 12-bit digitizer at a 250 kHz sampling rate. (Hereafter the ion saturation current fluctuation and the floating potential fluctuation are abbreviated as $\tilde{I}_{i,sat}$ and $\tilde{\Phi}_f$, respectively.)

The discharge conditions of the diverter plasmas are typically as follows: plasma current $I_p = 180$ kA, B_t at the plasma center $B_{t,0} = 1.1$ T, line averaged density $\overline{n}_e = 3\text{-}4 \times 10^{19}$ m^{-3}, the LCFS (last closed flux surface) position at midplane in low field side $R_{out} = 1.55$ m, the safety factor at the plasma center $q_0 \sim 0.55$, and the edge safety factor $q_{95} \sim 2.4$, respectively. The ion $\nabla \boldsymbol{B}$ drift direction is toward the X-point of the separatrix.

3.2 Quadratic spectra of floating potential fluctuations

Figure 2 (a) shows the auto-power spectra of $\tilde{\Phi}_f$. The spectra are calculated by fast Fourier transform (FFT) performed with a time window of 1 ms (1 kHz frequency resolution). Subtraction of the linear trend and multiplication by a window function were performed prior to FFT. In order to reduce the coefficient of variation, the calculated spectra were averaged over 40 time frames.

Two types of low-frequency fluctuations are observed in the auto-power spectra and the significant poloidal cross-coherence. One type has a coherent spectral peak around 15 kHz, and the other is the broadband fluctuations in the range of several tens of kHz. The coherent fluctuation is considered as the GAM [19, 28], and higher frequency components (frequency is higher than 30 kHz) are labeled as the broadband fluctuations. The spectral peak at the GAM frequency is observed only in $\tilde{\Phi}_f$, but neither in magnetic fluctuation dB_θ/dt (measured by on-vessel magnetic pick-up coils) nor in $\tilde{I}_{i,sat}$. The CMs are observed only inside the last closed flux surface (LCFS), not in the scrape-off layer (SOL). It is noted that, although the CMs appear in the majority of discharges, the CMs do not appear (in the RLP signal) in some discharges. At the position $r_s = 1.5$ - 2 cm, the amplitude of the CM ($|\tilde{\Phi}_{CM}|^2$) can be larger than the amplitude of the broadband fluctuations ($|\tilde{\Phi}_{bb}|^2$). r_s indicates the distance inside from the separatrix. The former $|\tilde{\Phi}_{CM}|^2$ is evaluated by integrating the power spectrum in the range of $|f - f_{CM}| \leq 5$ kHz.
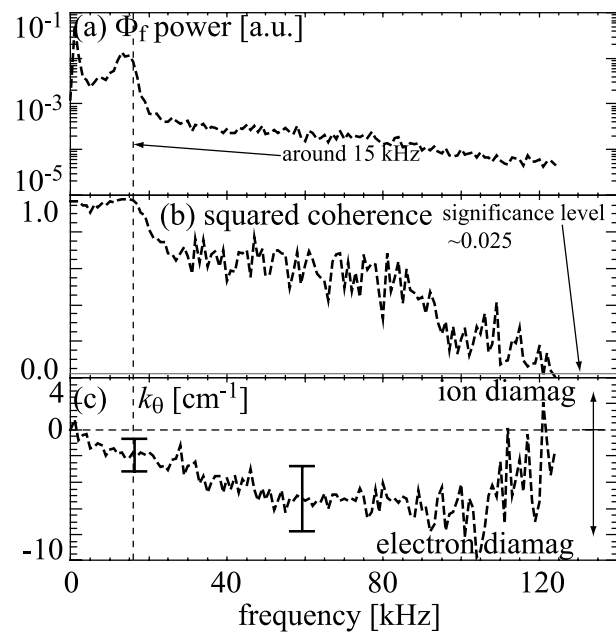

Fig. 2 Quadratic spectra of $\tilde{\Phi}_f$ at the location where the RLP is 2 cm inside the last closed flux surface (SN98327). (a) Auto-power spectra, (b) poloidal cross-coherence between two electrodes, and (c) k_θ calculated from poloidal cross-phase.

(f_{CM} is the central frequency of the CM, i.e., $\simeq 15$ kHz.) The latter $|\tilde{\Phi}_{bb}|^2$ is measured by the integral of the power spectrum in the range $22 < f < 125$ kHz. The cases of $1.8 < |\tilde{\Phi}_{CM}|^2/|\tilde{\Phi}_{bb}|^2 < 6$ are analyzed here. The condition that determines the appearance of the CMs has not yet been clarified. Further studies are necessary for investigating the generation condition.

In Fig. 2 (b), poloidal cross-coherence between $\tilde{\Phi}_{f,1}$ and $\tilde{\Phi}_{f,2}$ are shown. The coherence is almost 1 around the CMs and has significantly high values of ~0.6 at the background fluctuations. This high coherence supports the measurement of the cross-phase, providing an estimate of the poloidal wave number $k_\theta = \Delta\theta(f)/\xi_\theta$, where $\Delta\theta(f)$ is the phase difference between the Fourier components $\Phi_{f,1}$ and $\Phi_{f,2}$, and ξ_θ is the distance between the 1 and 2 probes in the poloidal direction, respectively. The large error bars seen in Fig. 2 (c) originate from the effect of the finite probe size relative to the distance between two electrodes. The distance between electrodes is about 2 or 3 times the electrode diameter. Calculated k_θ is inversely proportional to the possible distance between two electrodes. ($\xi_\theta = l \pm d$, where l or d are the distance between two electrode centers, or the diameter of the electrodes, respectively.) $\tilde{\Phi}_f$ of the background fluctuations has k_θ of ~4 cm^{-1} ($k_\perp\rho_s \sim 0.5$) and propagates in the electron diamagnetic drift direction.

The GAM oscillation appears as both potential ($\tilde{\phi}$) and density ($\tilde{n}$) fluctuations. However, the GAM fluctuation level in $\tilde{n}$ is smaller than that in $\tilde{\phi}$ [5]. The relationship between $\tilde{n}$ and $\tilde{\phi}$ in GAMs is reviewed in Ref [30], and the relative perturbation amplitude is theoretically given as

$$\frac{\tilde{n}_{GAM}}{n} = -\sqrt{2}q_r\rho_s \sin\Theta\left(\frac{e\tilde{\phi}_{GAM}}{T_e}\right), \qquad (6)$$

where q_r is the radial wavenumber of the GAMs, ρ_s is the ion Larmor radius at the electron temperature, and Θ is the poloidal angle of the observation position. Observing the coherence between signals identifies the density perturbation associated with the CMs. Figure 3 illustrates the power spectrum of $\tilde{\Phi}_f$, that in $\tilde{I}_{i,sat}$ and the squared coherence between these two. In Fig. 3 (a), a distinct peak in the spectrum at the CM frequency (around 15 kHz) is seen. In the power spectrum of $\tilde{I}_{i,sat}$, the peak at the CM frequency is obscure, as is expected from the theoretical prediction. Nevertheless, the small-but-finite density perturbation associated with the potential perturbation of the CMs is observable by measuring the coherence between $\tilde{\Phi}_f$ and $\tilde{I}_{i,sat}$. In Fig. 3 (c), a clear peak is observed at the CM frequency, showing that the CMs are associated with the small but finite coherent density perturbation. In addition, a significant squared cross-coherence at the background fluctuation is also observed in the range of 50 - 100 kHz. The phase difference between the potential fluctuation and the density perturbation is of interest for identifying the fluctuation mode. The phase and amplitude difference between $\tilde{n}$ and $\tilde{\phi}$ have been measured by the use of the HIBP [28, 31]. The phase difference between $\tilde{n}$ and $\tilde{\phi}$ was found to be con-
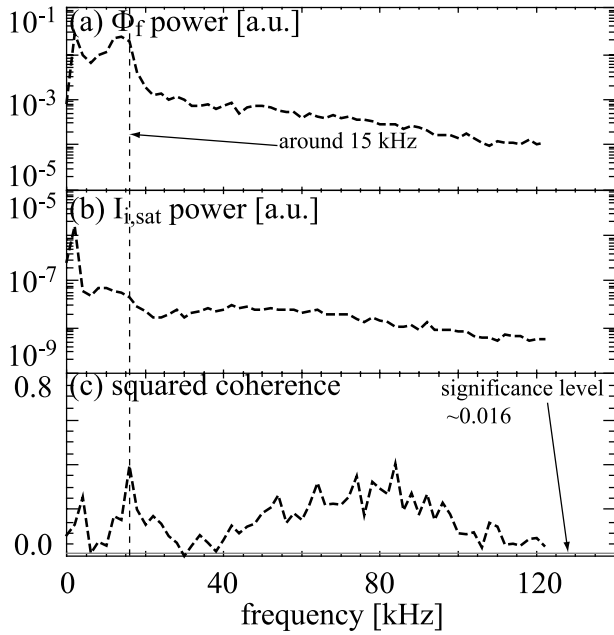
Fig. 3   (a) Auto-power of $\tilde{\Phi}_f$, (b) auto-power of $\tilde{I}_{i,sat}$, and (c) squared cross-coherence between $\tilde{\Phi}_f$ and $\tilde{I}_{i,sat}$. The frequency resolution is 2 kHz.

sistent with the prediction by the theory for GAMs, and the phase difference in the range of 50 - 100 kHz was around $(0.1 - 0.2)\pi$, confirming the predictions for drift waves.

Summarizing the measurement of second-order spectral functions, the CMs at ~15 kHz are conjectured to be GAM oscillations. Conclusive identification of GAMs requires precise measurement of the long-range correlations in the poloidal as well as toroidal directions. Keeping this in mind, a working hypothesis, that the CMs are GAMs, is used in comparing bispectral analysis with theoretical predictions in the following.

3.3   Results of bispectral analysis

It has been predicted that turbulence energy condenses into low frequency zonal flows by three-wave nonlinear couplings [5]. Energy transfer processes can be observed using bispectral analysis of potential fluctuations [16]. We show the squared bicoherence, which is an indicator of the nonlinear couplings, and the biphase, which shows the phase of nonlinear interaction of the three waves.

Figure 4 shows the squared auto-bicoherence of $\tilde{\Phi}_f$, $\hat{b}^2(f_1, f_2)$ (plotted in the $f_1 - f_2$ plane). The frequency resolution of bispectra is 1 kHz. In order to optimize the statistics, $\hat{b}^2(f_1, f_2)$ is calculated using 200 time frames. The details of the convergence study are given in a separate article [27]. Positive and negative values for f_2 indicate $f_3 = f_1 + |f_2|$ and $f_3 = f_1 - |f_2|$, respectively. The graph is symmetric with respect to the line $f_1 = f_2$ for $f_2 > 0$ and to the line $f_1 = -f_2$ for $f_2 < 0$. In Fig. 4, $\hat{b}^2(f_1, f_2)$ is clearly larger than that at other frequencies when f_1, f_2, or f_3 takes a value of around ± 15 kHz. The
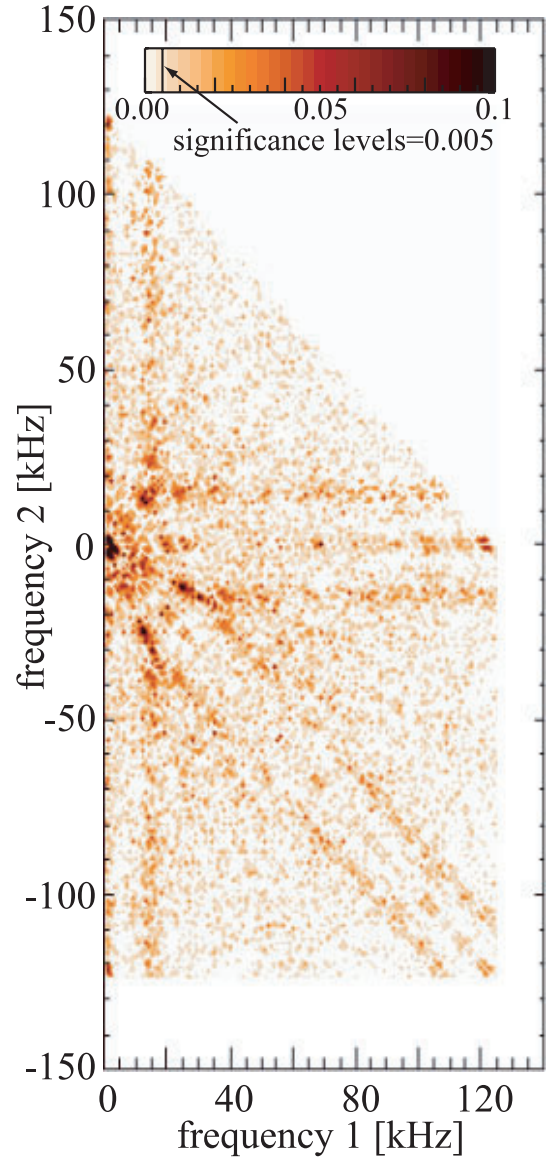

Fig. 4   Squared auto-bicoherence of $\tilde{\Phi}_f$ calculated using 200 realizations. The horizontal and vertical axes indicate f_1 and f_2, respectively. Intensities of the squared bicoherence are represented in the color bar.

average values of $\hat{b}^2(f_1, f_2)$ around 15 kHz are 0.02 - 0.05, while those of $\hat{b}^2(f_1, f_2)$ in other frequency area are around 0.01. The significance level of $\hat{b}^2(f_1, f_2)$, which is given by $1/M$ where M is the number of realizations in ensemble averaging [11], is 0.005, assuming that the variances of the auto-power spectra are negligible. Therefore, the value of $\hat{b}^2(f_1, f_2) = 0.1$ is above the statistical noise level.

Figure 5 shows the summation of the squared auto-bicoherence (the total bicoherence, $\Sigma \hat{b}^2(f_1, f_2)$) of $\tilde{\Phi}_f$ in the diverter plasmas. Summation is performed for a fixed value of f_3. The bispectrum in Fig. 5 is statistically admissible.

Other important information includes that regarding the biphase. Figure 6 shows the biphase on the (f_1, f_2)
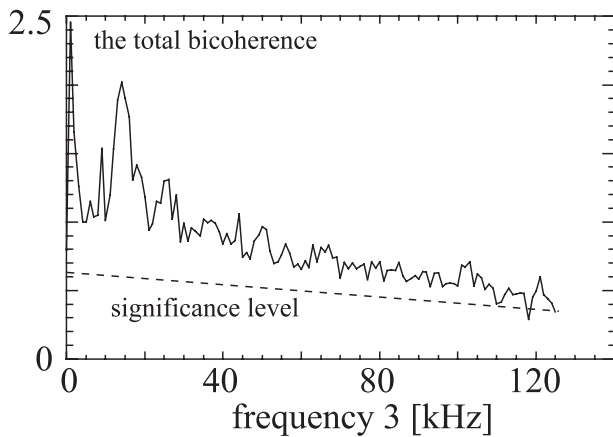
Fig. 5   Total squared auto-bicoherence of $\tilde{\Phi}_f$.

plane. The biphase derived from Eq. (5) ranges from $-\pi$ to π in Radian units. We have added 2π to the negative biphase, and the biphase is normalized by 2π for convenience. As a result, the range of the biphase is from 0 to 1, and a biphase of 0.5 indicates a point where the sign of the biphase changes. There is a symmetry in the biphase on the (f_1, f_2) plane as is understood from the definition of $\hat{B}(f_1, f_2)$. On the upper plane, $f_1, f_2 > 0$, the biphase is symmetric with respect to the interchange between f_1 and f_2. There is a noticeable trend in the biphase. That is, the biphase has a peaked profile near the frequency of CMs (e.g., f_1, f_2, or f_3 is close to ± 15 kHz). In contrast, the biphase is seemingly random for the mutual interactions of background drift wave fluctuations. When one observes the f_1 dependence for fixing the peak frequency f_2, the biphase change sign for $f_2 = +15$ kHz and $f_2 = -15$ kHz. This change of sign is also observed when one observes the f_1 for cases of $f_1 + f_2 = +15$ kHz and $f_1 + f_2 = -15$ kHz.

Such a difference of biphases at the CM frequency and at the broadband frequencies is more clearly demonstrated in Fig. 7. Figure 7 (a) illustrates the spectra of the biphase at the CM frequency (15 kHz, black closed squares), while those of the background fluctuations (50 kHz, gray closed squares) is given in Fig. 7 (b). The biphase for the case of the CM interaction with background fluctuations (i.e., $f_3 = 15$ kHz and f_1 and f_2 are varied over the broad band fluctuations) shows coherent peaks, and has a weak dependence on f_1 (e.g., for $f_1 > 60$ kHz, the biphase ~ 0.4, and for $60 > f_1 > 20$kHz, the biphase is 0.6 - 0.8). In contrast, the biphase for the mutual interactions of background turbulence (e.g., $f_3 = 50$ kHz and f_1 and f_2 are varied over the broad band fluctuations) spreads over the range of 0 and 2π. The biphases at the neighboring frequency of f_1 appear to be independent. Thus the biphase evidently discriminates the interaction between CMs and background fluctuations as well as the mutual interactions between background fluctuations.
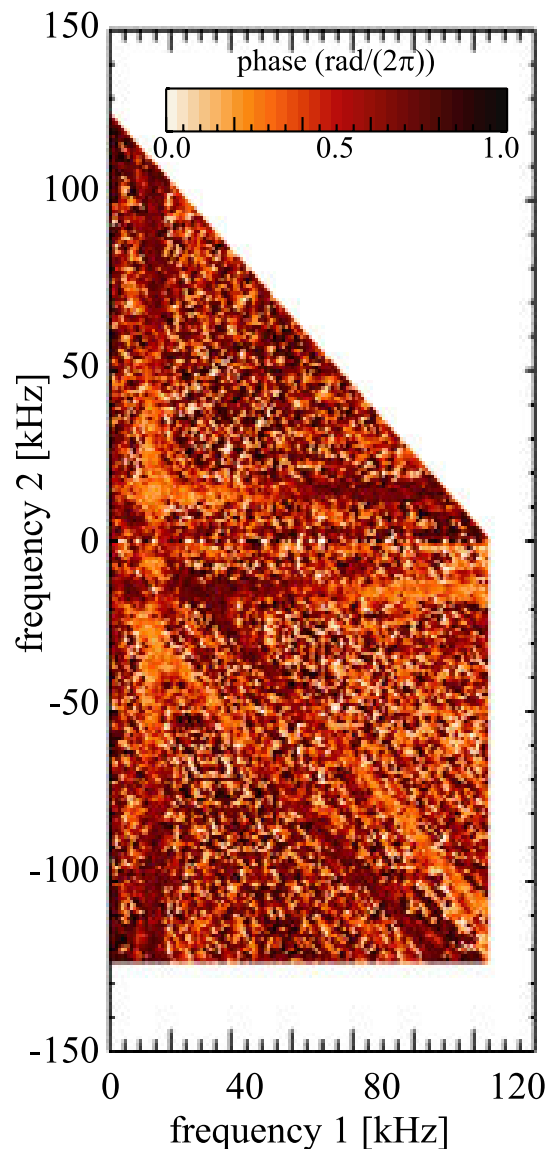

Fig. 6   Biphase plane in the diverter plasma. The horizontal and vertical axes indicate f_1 and f_2, respectively. Phase values of the biphase are represented in the color bar.

3.4   Discussion of the bispectrum data
3.4.1   Comparison between the diverter plasma and limiter plasma

In Fig. 4, $\hat{b}^2(f_1, f_2)$ around 15 kHz (for f_1, f_2, and f_3) is clearly larger than that at other frequencies. This feature is identical to limiter plasmas [25, 27]. The peak values of $\hat{b}^2(f_1, f_2)$ around 15 kHz are 0.02 - 0.05, giving small values in comparison with the limiter plasmas. This difference is also observed in the total bicoherence data. At the peak of the CM, the height is lower but the width is wider in the case of diverter plasmas in comparison with the limiter plasma. The area of the peak, above the level of the continuous component, is higher (by a factor of two or less) in the case of the diverter plasma. On the other hand, those of $\hat{b}^2(f_1, f_2)$ in other frequency area are around 0.01, and
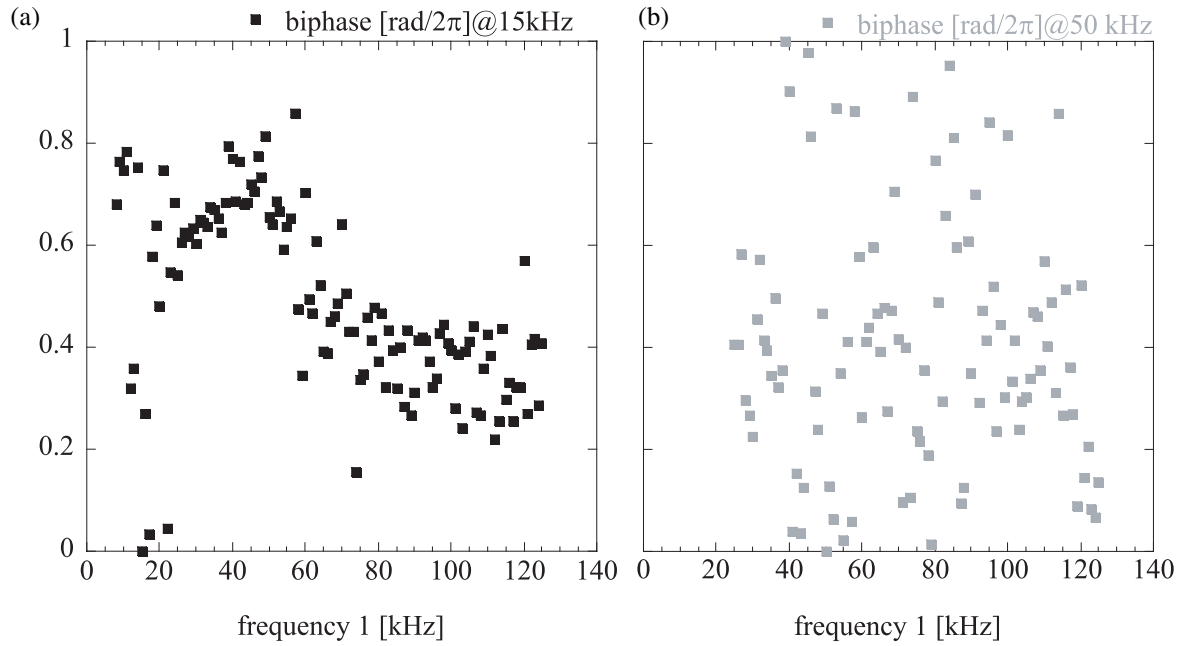
Fig. 7   Results of the biphase. (a) spectrum of biphase at 15 kHz, and (b) spectrum of biphase at 50 kHz, respectively. Horizontal axis denotes frequency 1 in Fig. 6

are similar to those in the limiter plasma. This difference in bicoherence at the peak CM frequency owes to the fact that CMs have wider full-width half-maximum in diverter plasmas. The biphase is concentrated in the vicinity of π near the CM frequency (for $f_3 > 60$ kHz). This feature is common to the limiter plasma, except for the difference of the frequency of CMs. In Ref. [32], the difference of the geodesic energy transfer from low frequency zonal flows to GAMs is discussed in regard to plasmas with and without an X point of the magnetic separatrix. The existence of the X point becomes geodesic curvature small, and as a result, the geodesic transfer in diverter plasmas could be smaller than that in limiter plasmas. In these experiments, because of poor statistics, we cannot discuss the difference of the absolute bicoherence values between limiter and diverter plasmas in coupling frequency between low frequency zonal flows and GAMs. We can test the geodesic transfer from bicoherence data if we have enough data and better statistical precision in future studies.

3.4.2   Comparison with theoretical predictions

An example of theoretical evaluations of the bispectrum of drift wave fluctuations was discussed in Ref. [22]. A normalized electrostatic potential, $\phi = (e\tilde{\phi}/T_e)L_n/\rho_s$, is introduced, where $\tilde{\phi}$ is the electrostatic potential fluctuation, ρ_s is the ion gyro-radius at electron temperature, and L_n is the density gradient scale length. (The normalized variable ϕ is of the order unity in stationary drift wave turbulence [1].) The one-field model (the Hasegawa-Mima model with the screening effect for the zonal flow component [5]) gives the response of drift wave in the presence of

zonal flow (pure zonal flow or GAMs) [22]. The acceleration rate of the test mode induced by the nonlinear interaction with the mode ϕ_ω, $\mathcal{N}\phi_\omega$, has been obtained, where

$$\mathcal{N} \simeq \frac{c_s}{L_n} \frac{k_r k_\theta k_\perp^2 \rho_s^4}{1 + k_\perp^2 \rho_s^2} \qquad (7)$$

for the mutual interactions between drift waves and

$$\mathcal{N} = \frac{c_s}{L_n} \frac{q_r k_\theta k_\perp^2 \rho_s^4}{1 + k_\perp^2 \rho_s^2} \qquad (8)$$

for the interaction between zonal flow and drift waves (ZF-DW). In these expressions, q_r is the radial wavenumber of the zonal flow, and $\mathbf{k}$ denotes the wavevector of the drift waves, while other notations are standard.

The first issue is the magnitude of the bispectrum. The observed intensity of the total bicoherence has been compared with the theoretical estimates of the limiter plasma [25]. It has been shown that the observed values can be explained by the theoretical evaluations. This conclusion holds for the diverter plasma as well, because the measured value of total bicoherence (either at the CM frequency or at the frequency background fluctuations) is of the same order of magnitude as that in limiter plasmas.

The other important issue is the biphase. Drift waves propagate in the poloidal direction, so that the sign of k_θ (poloidal wavenumber) is common to drift wave fluctuations. However, k_r (the wavenumber in the radial direction) can be either positive or negative, and the phase of $\mathcal{N}$ (for drift wave interactions, Eq. (7)) is considered to be random for each coupling combination. In contrast, the wavenumber q_r of a zonal flow is common to all interact-

ing drift waves. Thus, the phase of $\mathcal{N}$ (for ZF-DW interaction, Eq. (8)) is a common component of drift waves which interacts with zonal flows. This feature is an essential aspect for the modulational interaction of small-scale fluctuations. As is shown in [22], the biphase is a measure of the relative phase of the nonlinear acceleration rate. The observation of the biphase in this article clearly illustrates the contrast between the DW-ZF coupling (Fig. 7 (a)) and DW-DW coupling (Fig. 7 (b)). For the combination of $f_3 = 15\,\text{kHz}$, the biphase is weakly dependent on the frequency of the coupled mode (f_1) for $f_1 > 60\,\text{kHz}$. The reason for this weak dependence on f_1 has not yet been identified. (A conjecture is that it may owe to the finite gyro-radius effect and other effects, which are not taken into account in the reduced set of equations. Future research on this issue is necessary.) On the other hand, in the case of mutual coupling ($f_3 = 40\,\text{kHz}$), the biphase takes a seemingly random dependence on f_1. These observations confirm the theory of modulational nonlinear interaction of the ZF-DW system.

It should be noted that the convergence study is also indispensable for the biphase. The convergence study of the biphase has been reported in Ref. [27]. It was confirmed that the biphase at the peak CM frequency shows a close convergence even when the number of observation samples M is in the range of 100. The precise value for the biphase (in the case of mutual interaction of the broadband fluctuations) requires a larger number of observations. However, the seemingly random dependence on the frequency f_1 is not affected by the statistical variance of the biphase when M is of the order of 100.

4. Results from the CHS Device: Nonlinear Couplings in the H-Mode Plasmas

In this section, the results of bispectral analysis, as applied to the fluctuations of the edge plasmas in the Compact Helical System, are presented. After the transition to the high-confinement mode (H-mode) [33, 34], three types of fluctuations are observed: (i) coherent low frequency electromagnetic fluctuation, (ii) broadband fluctuations with the frequency range of 10 - 100 kHz, and (iii) high-frequency (above 100 kHz) broadband fluctuations. The coherent low-frequency fluctuation has been intensively studied [35]. This paper provides the first report on the nonlinear relationship between these three kinds of fluctuations. In Sec. 4.1, the layout of the study's diagnostics and discharge conditions are shown. In Sec. 4.2, experimental results are given regarding the discharge waveform and quadratic spectra. The auto-power spectra, poloidal cross-coherence, and cross-phase of floating potential fluctuations are shown. In Sec. 4.3, the results of bispectral analysis are presented.

4.1 Experimental setup of the CHS

The Compact Helical System (CHS) is a low-aspect-ratio middle size stellarator with a major radius $R_0 = 1\,\text{m}$, minor radius $a = 0.2\,\text{m}$, helical windings $l = 2$, and toroidal period number $N_t = 8$. In these experiments, the plasma's magnetic axis is located at $R_{\text{axis}} = 92.1\,\text{cm}$, and the toroidal magnetic field B_t is 0.88 T. The edge fluctuation measurements were performed by the use of hybrid probes (HP) [36]. Figure 8 illustrates the poloidal cross-section of the CHS device and the layout of the HP, together with the magnetic surfaces at three different β values. The flux surfaces are calculated using the VMEC code [37]. The HP head is made of oxygen-free copper, has a cylindrical form with a diameter of 40 mm, and is electrically isolated from the vacuum vessel. The HP insertion
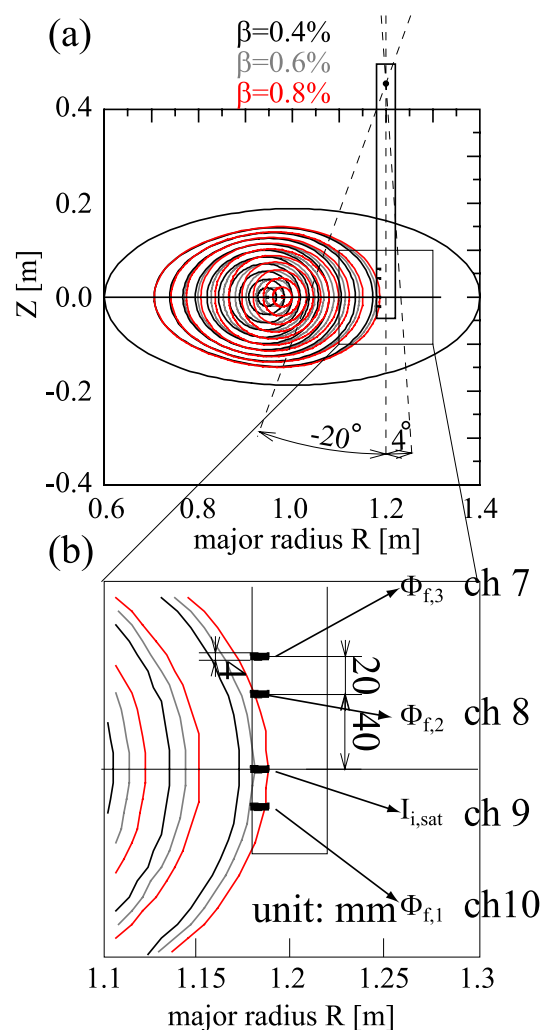

Fig. 8 (a) Layout of the diagnostics and the magnetic flux surface (MFS) of typical H-mode plasmas on CHS. Black contour lines indicate the MFS of β=0.4 % plasmas, gray contour lines indicate that of β=0.6 % plasmas, and red contour lines indicate that of β=0.8 % plasmas, respectively. (b) Enlarged view of the vicinity of the hybrid probe head. Usage of each channel in the experiments is also shown.

axis can be inclined (on the poloidal plane) from the vertical axis in the range of −4 to 20 degrees. The electrode-mounting surface is rotatable around the insertion axis. The HP has ten electrodes arranged linearly along the HP head at an interval of 20 mm. The cylindrical electrodes (with a diameter of 4 mm and a height of 1 mm) are made of copper. In the experiments, four electrodes at the end of the HP head were used. One electrode is used for the ion saturation current fluctuation ($\tilde{I}_{i,sat}$) measurement, and the other three electrodes are used for measuring the floating potential fluctuations $\tilde{\Phi}_f$ (see Fig. 8 (b)). Analog signals from the HP are low-pass filtered by a fourth-order Bessel filter with a cutoff frequency of 100 kHz, and are digitized by a 14-bit digitizer at a 1 MHz sampling rate.

4.2 Time evolutions of CHS waveforms and signals from the HP

Figure 9 shows the time evolutions of the waveforms of the CHS H-mode plasmas and signals from the HP. The L-H transition in CHS is characterized by a drop of H_α intensities (Fig. 9 (a)) as indicated by the dashed vertical
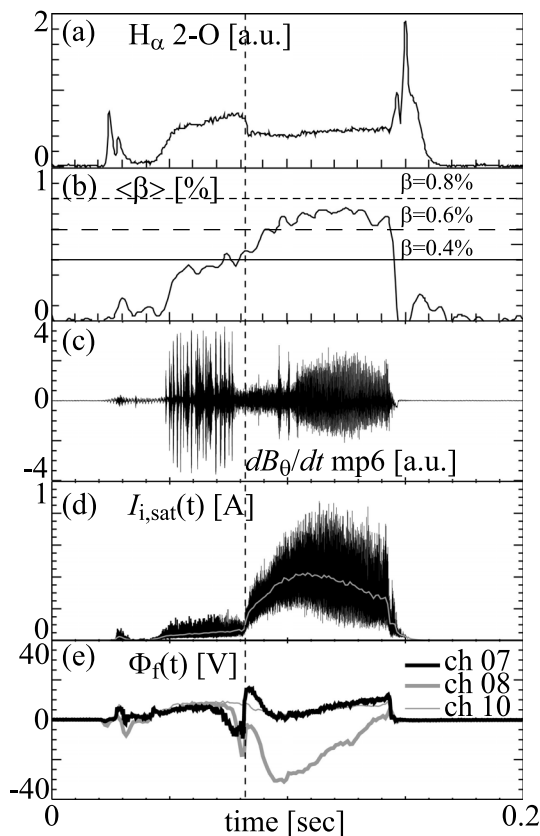

Fig. 9   Time evolutions of waveforms from CHS plasmas. (a) Intensities of H_α emission, (b) $\langle\beta\rangle$, (c) dB_θ/dt measured by on-vessel magnetic pickup coil, (d) $I_{i,sat}(t)$ measured by channel 9 electrode, and (e) $\Phi_f(t)$ (low-pass-filtered, $f < 1$ kHz) measured by three electrodes, respectively. Dashed vertical line indicates timing of L-to-H transition. In Fig. (d), $\tilde{I}_{i,sat}$ ($f < 1$ kHz) is shown as a gray line.

line. The ion saturation current $I_{i,sat}$, measured by channel 9, is shown in Fig. 9 (d). It has a stationary mean value and stationary fluctuation amplitude in the L-phase. After the transition, $I_{i,sat}$ starts to increase rapidly. The floating potential Φ_fs of channels 7 and 8 gradually become negative in advance (by about ∼30 msec) before the transition (the pre-transition phenomenon). In L-mode discharges, the pre-transition phenomenon is not observed. Just after the transition, Φ_f of channel 8 becomes negative after a short jump to smaller negative values. In contrast, Φ_fs of channels 7 and 10 do not have negative values even after the transition. Among probes 7, 8 and 10, probe 8 is placed on the inside magnetic surface, probe 10 is next, while probe 7 is placed on the outer magnetic surface after the L-H transition. Thus, a steep negative radial electric field is apparently established (in the H-mode phase) inside the magnetic surface where probe 10 is placed. This suggests that the negative radial electric field near the plasma surface may have a very complex radial profile. (This interpretation is based on the assumption that the mean electrostatic potential on a magnetic surface is constant. A recent theory has predicted the inhomogeneity of the mean electrostatic potential on the magnetic surface for the H-mode plasmas [38]; Thus, more detailed measurement is required in order to determine the radial electric field structure of the H-mode plasmas.)

4.3 The quadratic spectra in H-mode

Figure 10 illustrates the data of the quadratic $\tilde{\Phi}_f$ spectra during H-mode. (The time window is from 100 ms to 104 ms in Fig. 9.) All spectra are calculated using the same procedure as results of JFT-2M. Frequency resolution is 0.244 kHz. The auto-power spectra in both the linear and logarithmic scales are shown in Fig. 10 (a). There are three types of fluctuations. The first is a sharp spectral peak around 4 kHz (abbreviated as type A). Type A fluctuation is observed in three different physical parameters, i.e., $\tilde{I}_{i,sat}$, $\tilde{\Phi}_f$, and the magnetic fluctuations measured near the chamber wall (see Fig. 10 (d) for the magnetic fluctuations). The properties of type A fluctuation have been studied by measuring density fluctuations, and has been reported by Oishi, et al.[35]. In these series of discharges, the type A fluctuation does not always appear in the H-mode phase, but appears in the time-window from 100 to 140 msec. (The threshold condition for the onset of this fluctuation has been observed.) The second type of fluctuation is the broadband fluctuation in the range from 10 to 100 kHz (abbreviated as type B). There is no clear correlation between magnetic fluctuations and type B fluctuations, suggesting that type B is an electrostatic mode. The third type is the other broadband fluctuation with spectral peaks around 300 - 400 kHz (abbreviated as type C). (Owing to the filter effect at high frequency, the intensity of the type C fluctuation in Fig. 10 (a) is reduced in comparison with that of the type B.) Type C correlates clearly with magnetic
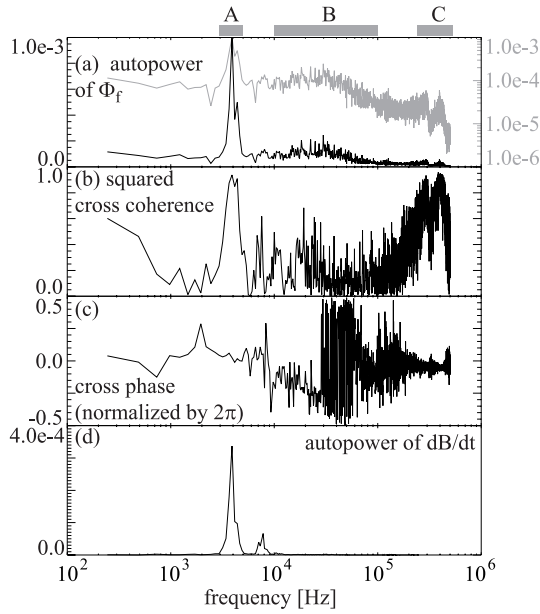
Fig. 10 Quadratic $\tilde{\Phi}_f$ spectra during H-mode. (a) Auto-power spectra, (b) squared cross-coherence of $\tilde{\Phi}_f$ between channel 10 and channel 7, (c) cross-phase same as (b), (d) auto-power spectra of dB_θ/dt. Gray line in Fig. (a) indicates same plots as black line in logarithmic scale. Gray rectangles at the top of figures and abbreviations A, B, and C indicate classification for fluctuations in the three frequency ranges addressed in this paper.

fluctuations. Because of the limitation of the data sampling, we cannot identify types B and C fluctuations. This paper shows linear and nonlinear properties of the fluctuations and will face on identifying these modes in future studies.

This classification of three types of fluctuations becomes more evident by observing the spatial cross-coherence and cross-phase spectra in Fig. 10 (b) and (c). Figure 10 (b) illustrates the cross-coherence between the potential fluctuation signals measured by probes 7 and 10. (These two probes are separated by the distance of 8 cm.) For types A and C fluctuations, the cross-coherences across the 8 cm-distance have significantly high values of ∼0.9. The cross-phases are almost 0. These results indicate that types A and C fluctuations have long correlation length (much longer than 8 cm). However, the radial and poloidal wavenumbers have not yet been evaluated. Detailed studies are necessary for clarifying poloidal/radial wavenumbers. In contrast, the cross-coherence of type B is relatively small (less than 0.3), suggesting that type B has a short correlation length.

4.4 Results of the bispectral analysis
4.4.1 Bispectrum

Figures 11 show the squared auto-bicoherence plane $\hat{b}^2$ of $I_{i,sat}$. The frequency resolution is 0.244 kHz. In order to optimize the statistics, $\hat{b}^2$s are calculated using

110 time frames obtained from all H-mode phase data in 4 similar discharges. The realization number is not sufficient for obtaining converged bicoherence. Nevertheless, auto-bicoherence that is higher than the significance level was obtained. Thus, a semi-quantitative conclusion can be drawn. The significance level is 0.009. The magnitude of the bicoherence is expressed in terms of different colors. From this figure, the following nonlinear couplings among three types of fluctuations can be detected:

    i) type A and B,
    ii) type A and C,
    iii) type B and C,
    iv) among type B, and
    v) among type C.

The coupling (i) is observed in the domain

$$|f_1 + f_2| < 5\,\text{kHz and } f_1 < 100\,\text{kHz}.$$

The combination (ii) is seen in the domain

$$|f_1 + f_2| < 5\,\text{kHz and } f_1 > 100\,\text{kHz}.$$

The coupling (iii) is seen in the domains

$$5 < |f_1 + f_2| < 100\,\text{kHz and } f_1 > 100\,\text{kHz}.$$

Next, (iv) appears in the domains

$$5 < |f_1 + f_2| < 100\,\text{kHz and } 5 < f_1 < 100\,\text{kHz}.$$

Finally, (v) is presented in the regions

$$|f_1 + f_2| > 100\,\text{kHz and } f_1 > 100\,\text{kHz}.$$

Combinations (i) and (ii) reveal the interaction between the coherent and global fluctuation (type A) and the high-frequency and broadband fluctuations (B or C). Combination (iii) indicates the interactions among broad-band (and different kind) fluctuations. Combinations (iv) and (v) denote the self-nonlinear interactions among broadband fluctuations.

Three characteristic domains are highlighted by boxes and a circle in Fig. 11. Figure 11 (b) is an expanded view for the low frequency region (the horizontal frequency 1 ranges from 0 to 100 kHz, and the vertical frequency 2 ranges from −100 to 0 kHz). In this expanded domain, combinations (i) and (iv) are shown in detail. Signals above the significance level are demonstrated. Unambiguous coupling between types A and B is seen. The nonlinear coupling among type B fluctuations is also observed. (These are qualitatively similar to the case of GAM and drift wave fluctuations in JFT-2M plasma.)

The other characteristic area is highlighted in the high frequency region, (Fig. 11 (c)) in horizontal frequency 1 ranging from 300 to 400 kHz, and in vertical frequency 2 ranging from −400 to −300 kHz. This expanded graph illustrates couplings (ii) and (iii). Significant nonlinear couplings between the coherent fluctuation (type A) and the
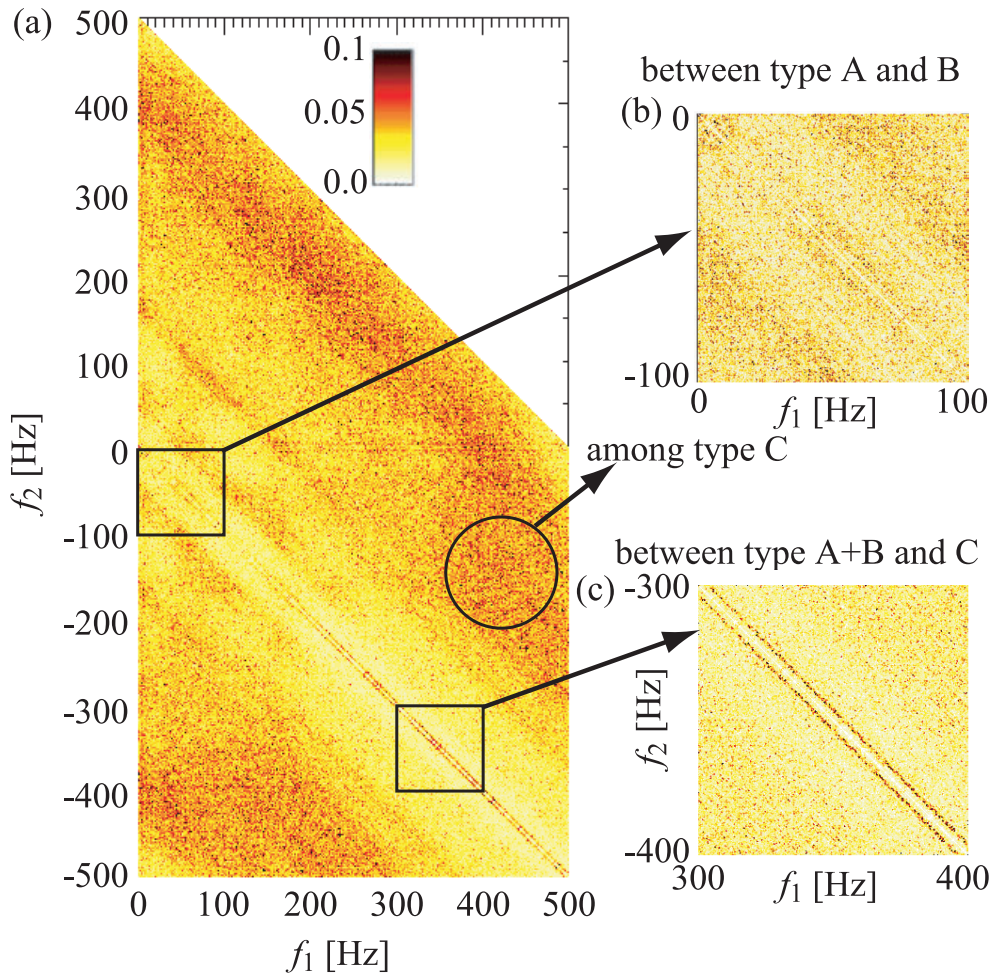
Fig. 11 The squared bicoherence plane of $\tilde{I}_{i,sat}$ during H-mode. (a) Full range plots, (b) enlarged view in the horizontal range from 0 to 100 kHz, and in the vertical range from -100 kHz to 0 kHz, and (c) enlarged view in the horizontal range from 300 to 400 kHz, and in the vertical range from -400 kHz to -300 kHz, respectively. Two rectangles with black lines in Fig. (a) indicate the areas of enlarged view of (b) and (c).

broadband (type C) fluctuations are clearly observed. The coupling between them is unambiguous. In contrast, nonlinear couplings between type B and type C fluctuations are not significant.

A black circle in Fig. 11 (a) emphasizes the bicoherence of coupling (v). Relatively strong nonlinear couplings are observed. This indicates that type C fluctuations are nonlinearly coupled to each other.

4.4.2 The total bicoherence

Figures 12 (a) and (b) show the total auto-bicoherence spectra of $\tilde{I}_{i,sat}$ and $\check{\Phi}_f$. Spectral data are chosen from the range where coherent type A fluctuation appears in similar 4 discharges same as Fig. 11. The time window of the data becomes shorter, because the type A fluctuation appears in a later phase of the H-mode, where the pressure gradient exceeds the threshold for the onset of the type A fluctuation [35]. As a consequence of the reduction of the length of time window, the realization number is limited to 48.

Figures 12 (c) and (d) show the auto-power spectra of $\tilde{I}_{i,sat}$ and $\check{\Phi}_f$.

Before discussing the total bicoherence for the CHS plasmas in Figs. 12, a brief note is commented on the difference (in absolute values) from the total bicoherence in the JFT-2M results which is shown in Fig. 5. This difference in magnitude is caused by the difference in the numbers of realization and frequency segments. Realization number M and the number of frequency segments N in the analysis of the JFT-2M data are 200 and 250, respectively, while those in the analysis of the CHS data are 48 and 2048, respectively. (The frequency segment N is given by the ratio between the upper frequency boundary (500 kHz for the CHS case) and the frequency resolution (0.244 kHz for the CHS case).) The significance level of the total bicoherence is given approximately by N/M. That is, in this article it is 2048/48=42.7 for the CHS and 125/200=0.625 for JFT-2M data. The signal of the total bicoherence increases (for the given strength of the nonlinear interaction
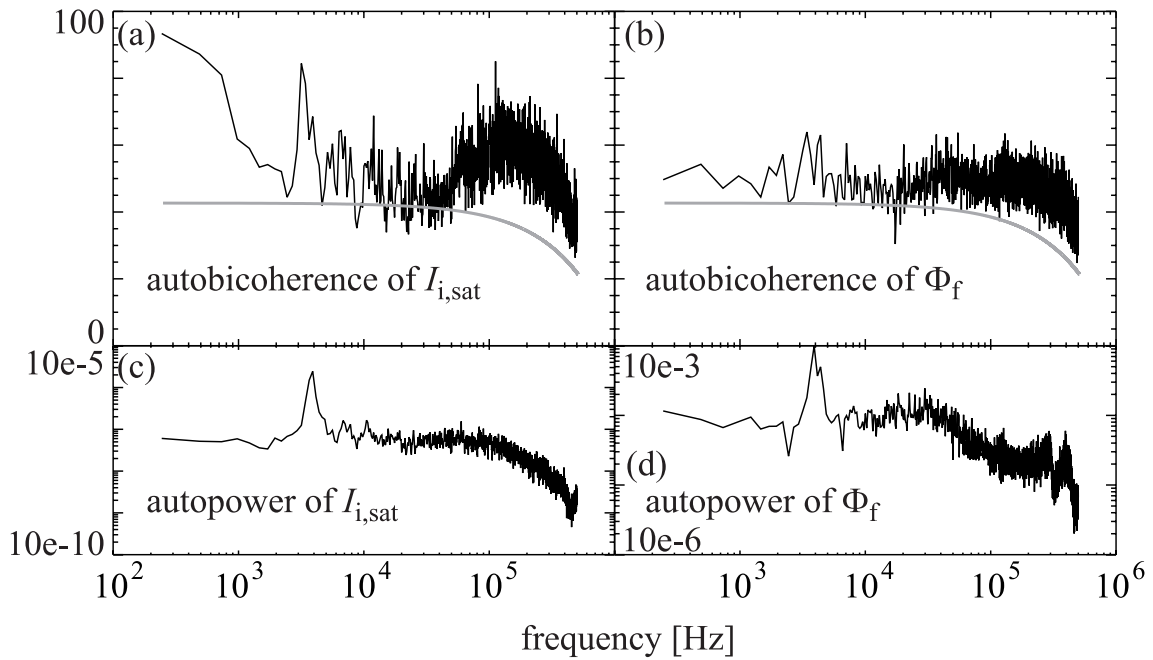
Fig. 12 Total squared bicoherence spectra and auto-power spectra during H-mode. (a) total bicoherence of $\tilde{I}_{i,sat}$, (b) total bicoherence of $\tilde{\Phi}_f$, (c) auto-power spectra of $\tilde{I}_{i,sat}$, and (d) auto-power spectra of $\tilde{\Phi}_f$, respectively. Gray lines in Figs. (a) and (b) indicate the significance levels.

and for the given amplitude of the coherent fluctuations) if the N frequency segments increase [22]. Thus, the difference in the number of frequency segments N leads to the differences of the total bicoherence data and the significance level in two experiments (Fig. 5 and Fig. 12). Note that the significance level of the total bicoherence becomes smaller as the frequency becomes high in Fig. 12. Under the constraint that the frequency range is limited to below 500 kHz (in the CHS case), the number of combinations that satisfies $f_1 + f_2 = f_3$ becomes smaller than 2048 as the target frequency f_3 increases. This causes the reduction of the significance level in the high frequency region.

From the observation of Fig. 12, we have the following conclusion for the total bicoherence of edge fluctuations of CHS plasmas.

We first investigate the bicoherence of type A. For the low-frequency coherent component, a very clear peak appears in the total bicoherence of the $I_{i,sat}$ spectra. As well, the peak at type A exists, in the total bicoherence of $\tilde{\Phi}_f$. However, the peak in Fig. 12 (b) at the frequency of type A is weaker than that seen in Fig. 12 (a). The total bicoherence shown in Fig. 12 is not completely converged owing to the limited number of realizations M. The estimate of error has been previously performed in a convergence study [27]. The 'significance level' in Fig. 12 denotes the statistical variance which converges in proportion to $1/M$. When the statistical variance becomes smaller than the real signal, the difference between the observed bicoherence and the converged value was found to be close to the significance level [27]. Thus, in such a situation, the dif-

ference between the calculated total bicoherence and the significance level is used as an estimate of the real total bicoherence. Based on this convergence study, the difference between the total bicoherence of the density fluctuation spectrum (Fig. 12 (a)) and that in the potential fluctuation spectrum (Fig. 12 (b)) is analyzed. An estimate of the total converged bicoherence in the density fluctuation is about 40, while that in the potential fluctuation is about 15. Thus, the total bicoherence is three-times larger for density fluctuations than for potential fluctuations in the nonlinear coupling of type A fluctuations.

Next, the properties of type B fluctuations are seen in the intermediate domain (10 to 100 kHz) of Fig. 12. The calculated total bicoherence is close to the significance level. The calculated value is larger for the potential fluctuation spectrum than for the density perturbation. The calculated value of auto-bicoherence for the potential fluctuation is larger than the significance level, and the nonlinear interaction, in which type B fluctuations play a role, is captured in this figure. However, the signal level is not high enough to draw a quantitative conclusion regarding the intensity of the nonlinear interaction of this range of fluctuations.

It is striking that the total bicoherence in the frequency range of type C fluctuations is significant. In particular, the auto-bicoherence of the density fluctuation spectrum is unambiguous. By subtracting the significance level from the calculated auto-bicoherence of the density fluctuation spectrum, one obtains the estimate for the auto-bicoherence. The estimated value is around 30, which is

as strong as that for the type A component. As is the case of type A, the calculated auto-bicoherence is weaker in the total bicoherence spectra of $\tilde{\Phi}_f$. Thus, the nonlinear interaction for type C fluctuations is considered to function not mainly through the electrostatic potential fluctuation but mainly through other dynamical variables of plasmas. It should be commented here that the attenuation of the data signal at high frequency owing to the filter does not influence the present conclusion. As is understood from the definition Eq. (3), the attenuation of the data signal is cancelled in calculating the total bicoherence.

4.5 Discussion of the observed bispectrum

We here briefly discuss possible interpretations of the observed bicoherence data of CHS plasmas.

In this study, the auto-bispectrum is calculated for the density perturbation and potential perturbation simultaneously. As a result, we found a noticeable difference between the auto-bispectrum of density fluctuation and that of the potential fluctuation for type A fluctuations. Based on magnetic fluctuation measurement (outside of the plasma), type A is considered to be a coherent MHD fluctuation with a long wavelength [35]. For coherent MHD fluctuations in toroidal plasmas, the frozen-in condition is approximately satisfied (except for a particular location such as the reconnection point). In the low-β discharge discussed here, the magnetic perturbation is represented by $\tilde{B}_r$ ($\tilde{B}_\theta$ is deduced from it by use of the divergence-free condition for magnetic field perturbations), and the frozen-in condition relates the density and magnetic field perturbations as $\tilde{n}/n_0 \simeq -i(\tilde{B}_r/B_0)k_{//}^{-1}L_n^{-1}$ where L_n is the density gradient scale length. Thus, the density perturbation in the coherent MHD perturbation reflects the magnetic field perturbation. The parallel electric field vanishes approximately due to the high electric conductivity; i.e., the relation $\tilde{B}_r \simeq (ik_\theta k_{//}/\omega)\tilde{\phi}$ holds ($\tilde{\phi}$: the electrostatic potential perturbation). One has a relation

$$\frac{\tilde{n}}{n_0} \simeq \frac{\omega_*}{\omega}\frac{e\tilde{\phi}}{T_e}. \tag{9}$$

For the coherent MHD fluctuations with $\omega_* > \omega$, the relative density perturbation can be larger than the electrostatic potential perturbation. (For the present situations, one can choose values $T_e = 50\text{-}100\,\text{eV}$, $L_n = 3\,\text{cm}$, and $m = 1$ to obtain a range $\omega_* = 6\text{-}10\,\text{kHz}$, suggesting that ω_* is twice the real frequency of the observed coherent fluctuation, type A). Under this circumstance, the density perturbation represents the presence of the magnetic field perturbation. The nonlinearity, which is observed in the auto-bicoherence of the density perturbation spectrum, can be interpreted as the nonlinearity associated with the pressure gradient or the Lorentz force in the equation of motion. The comparison of the peaks (at type A) in Figs. 12 (a) and (b) indicates that the nonlinearity associated with the $E \times B$ motion owing to the electrostatic potential perturbation is weaker than those owing to the combinations of the

Lorentz force and the pressure perturbations.

One can also draw an estimate of the magnitude of the nonlinear interaction between the coherent component (type A) and broadband fluctuations (type C). According to the theoretical analysis of the interaction between the coherent perturbation and the broadband fluctuations [22], the squared bicoherence is estimated as

$$\hat{b}^2(\omega,\, p) \sim 4\tau_{p-\omega}^2|\mathcal{N}_{p-\omega,\, p}g_\omega|^2, \tag{10}$$

where ω is the frequency of coherent fluctuation, p is the frequency of the broadband fluctuations, $\tau_{p-\omega}$ is the auto-correlation time of the beat mode (frequency $p - \omega$), g_ω is the Fourier amplitude of the coherent fluctuation, and $\mathcal{N}_{p-\omega,\, p}g_\omega$ is the acceleration rate for the beat mode owing to the interaction of the ω- and p- modes. Figure 11 (c) illustrates that $\hat{b}^2(\omega,\, p)$ is of the order of 0.05 for the interaction between type A (which is labeled ω in this theoretical formula) and type C (which is labeled p or $p - \omega$, because $p \gg \omega$ holds). Therefore, the measurement of $\hat{b}^2(\omega,\, p) \sim 0.05$ provides an interpretation

$$|\mathcal{N}_{p-\omega,\, p}g_\omega| \sim 0.1\tau_p^{-1}, \tag{11}$$

where $\tau_p \sim \tau_{p-\omega}$ is used. That is, the nonlinear frequency modulation of the broadband fluctuation (type C) by the coherent low frequency mode (type A) is of the order of one-tenth of the decorrelation rate of the high-frequency fluctuations (which is determined by, e.g., the mutual nonlinear interactions among type C fluctuations). Thus this measurement provides a clue for experimentally estimating the nonlinear effect of the coherent mode on high frequency fluctuations.

The other important finding is the significant bicoherence for the high-frequency component (type C). The bicoherence for the broadband fluctuations was analyzed, and the total bicoherence was found to be proportional to the square of the ratio of the nonlinear coupling coefficient between different Fourier components to the characteristic auto-correlation time of broad-band fluctuations. The significant auto-bicoherence is observed in the auto-bicoherence of the density perturbation spectrum, and the total bicoherence is weaker for the potential fluctuation than for the density perturbation. This demonstrates that the nonlinear interactions among the type C are now experimentally observed. At this moment, however, the spatial structure of the high frequency fluctuation (type C) has not yet been observed. Therefore, one cannot draw a conclusive interpretation of the total bicoherence for the type C fluctuations. One working hypothesis is that the nonlinear interaction is stronger through the density perturbation (i.e., via the pressure perturbation or the Lorentz force) than through the convective nonlinearity associated with the $E \times B$ motion induced by the electrostatic potential. Type C is observed in magnetic fluctuations, and is observed in both density and potential. There is significant correlation between them and cross-bicoherence be-

tween density and potential is also significant. The cross-bicoherence provides information of particle flux if density and potential are measured in same location. In this paper, auto-bicoherence analysis is presented in order to test electrostatic/electromagnetic features of fluctuations, and results from cross-bicoherence analysis will be presented in future step.

5. Summary and Discussion

In summary, we have reported the application of the bicoherence analysis to the edge plasmas of JFT-2M and CHS. In both cases, the fluctuations are composed of the coherent modes (CMs) and broadband fluctuations. By measuring the bicoherence spectrum, the intensity and the phase of the nonlinear interaction were experimentally estimated. These results have contributed to the progress in understanding plasma turbulence quantitatively.

In the case of the JFT-2M plasma, attentions were made at the CMs near the frequency of the geodesic acoustic modes (GAMs) and at the broadband fluctuations, which are attributed to the drift wave fluctuations. In this study, the nonlinear interactions between the CMs and broadband fluctuations, and those among broadband fluctuations (like-scale interaction) were analyzed. The biphase for the diverter plasmas was investigated for the first time. The common phase in the biphase indicates that the broadband fluctuations interact with the CMs with a well-defined phase. This supported the theoretical prediction, that the CMs like GAMs are excited by the modulational interaction of drift waves with the test GAMs [5]. The intensity of the total bicoherence for CMs and broadband fluctuations were compared with theoretical estimate. The result was consistent with the model, in which the convective nonlinearity by the $E \times B$ motion is the main nonlinear interactions.

In the case of the CHS plasma, the method was extended so that both the auto-bicoherence of the density perturbation and that of potential fluctuation were obtained. In the CHS plasma, the edge fluctuations are composed with three elements: the coherent low-frequency oscillation which is attributed to an MHD mode (type A), the broadband fluctuations which are attributed to the drift wave fluctuations (type B), and the high frequency fluctuation, which may be associated with electromagnetic perturbations (type C). As was the case of the JFT-2M plasma, the sharp peak appears in the bicoherence at the frequency of type A component. The interactions of type A with B and C were unambiguously confirmed. The nonlinear coupling among the broadband fluctuations type B and that among type C were confirmed, showing that mutual interaction among B and that among C are important for the evolution of type B and type C, respectively. However, the cross-interaction between the type B and type C was found weak, compared to other combinations. The difference of auto-bicoherence among combinations of the fluc-

tuations provides a key to distinguish the nonlinear interactions among different type of fluctuations. The convergence of the total bicoherence for the CHS plasma, in this article, is poorer than that for the JFT-2M plasma. Thus the reported value of the bicoherence is yet with a substantial error. However, as a first step of the analysis, an estimate was obtained for the magnitude of the nonlinear Doppler shift for the high-frequency fluctuations owing to the presence of the low frequency CMs in the CHS plasma.

The studies on JFT-2M plasmas, by use of the bicoherence analysis, suggest that the nonlinearity associated with the $E \times B$ convection of vortex motion plays an important role of nonlinear interaction among drift waves and GAMs. It is true that other nonlinear effects (e.g., those in pressure and Lorentz force dynamics) exist. Studying the CHS plasmas highlighted such varieties of nonlinear interaction. In this case, the CM was attributed to the MHD mode. The peak of the auto-bicoherence (at CM frequency) was found to be more prominent for the density fluctuation spectrum than for the potential fluctuation spectrum. This is interpreted that the nonlinear interaction through either pressure or Lorentz force is stronger than that through the $E \times B$ motion owing to the potential perturbation. This study has illustrated the possibility of separating various kinds of nonlinear interactions by observing the various auto-bicoherence as well as the cross-bicoherence. The observation of the squared bicoherence has provided the experimental estimate for the nonlinear interaction between the CM and the broadband fluctuations. This result provided the basis for the future comparison study with theory.

It is also stressed here that the broadband fluctuations in the range of 100 - 500 kHz have shown unambiguous nonlinear couplings among themselves. That is, these fluctuations possibly contribute to the mean transport (i.e., the turbulent particle and turbulent thermal transport). This also stimulates the intensive studies of the high-frequency broadband fluctuations, in addition to the medium-frequency broadband fluctuations. These are left for future studies.

Acknowledgments

[1] K. Itoh, Nucl. Fusion **43**, 1710 (2003).

[2] K. Itoh, S.-I. Itoh and A. Fukuyama, *Transport and Structural Formation in Plasmas* (Institute of Physics Publishing, Bristol and Philadelphia, 1999).

[3] A. Yoshizawa, S.-I. Itoh and K. Itoh, *Plasma and Fluid Turbulence: Theory and Modelling* (Institute of Physics Publishing, Bristol and Philadelphia, 2003).

[4] J. Krommes, Phys. Reports **360**, 1 (2002).

[5] P. Diamond, S.-I. Itoh, K. Itoh and T. Hahm, Plasma Phys. Control. Fusion **47**, R35 (2005).

[6] Z. Lin, T. Hahm, W. Lee *et al.*, Science **281**, 1835 (1998).

[7] C. Holland, G. Tynan, P. Diamond *et al.*, Plasma Phys. and Control. Fusion **43**, 1055 (2001).

[8] S.-I. Itoh, K. Itoh and M. Yagi, Phys. Rev. Lett. **91**, 045003 (2003).

[9] M. Yagi, S. Yoshida, S.-I. Itoh *et al.*, Nucl. Fusion **45**, 900 (2005).

[10] M. Hino, *Spectral Analysis* (Asakura Shoten, Tokyo, 1977), [*in Japanese*].

[11] Y. Kim and E. Powers, IEEE Trans. Plasma Sci. **PS-7**, 120 (1979).

[12] C. Ritz, H. Lin, T. Rhodes and A. Wootton, Phys. Rev. Lett. **65**, 2543 (1990).

[13] B. van Milligen, E. Sánchez, T. Estrada *et al.*, Phys. Plasmas **2**, 3017 (1995).

[14] B. van Milligen, C. Hidalgo, E. Sánchez *et al.*, Rev. Sci. Instrum. **68**, 967 (1997).

[15] P. Diamond, M. Rosenbluth, E. Sánchez *et al.*, Phys. Rev. Lett. **84**, 4842 (2000).

[16] G. Tynan, R.A. Moyer, J. Burin and C. Holland, Phys. Plasmas **8**, 2691 (2001).

[17] R. Moyer, G. Tynan, C. Holland and M. Burin, Phys. Rev. Lett. **87**, 135001 (2001).

[18] C. Holland, G. R. Tynan, P. H. Diamond *et al.*, Plasma Phys. and Control. Fusion **44**, A453 (2002).

[19] Y. Nagashima, K. Hoshino, A. Ejiri *et al.*, Phys. Rev. Lett. **95**, 095002 (2005).

[20] G. Xu, B. Wan and M. Song, Phys. Plasmas **9**, 150 (2002).

[21] A. Fujisawa, K. Itoh, H. Iguchi *et al.*, Phys. Rev. Lett. **93**, 165002 (2004).

[22] K. Itoh, Y. Nagashima, S.-I. Itoh *et al.*, Phys. Plasmas **12**, 102301 (2005).

[23] Y. Kusama, M. Yamamoto and JFT − 2M Group, Fusion Sci. Tech. **49**, 89 (2006).

[24] N. Winsor, J. Johnson and J. Dawson, Phys. Fluids **11**, 2448 (1968).

[25] Y. Nagashima, K. Itoh, S.-I. Itoh *et al.*, Plasma Phys. Control. Fusion **48**, S1 (2006).

[26] D. Grésillon and M.S. Mohamed-Benkadda, Phys. Fluids **31**, 1904 (1988).

[27] Y. Nagashima, K. Itoh, S.-I. Itoh *et al.*, Rev. Sci. Instr. **77**, 045110 (2006).

[28] T. Ido, Y. Miura, K. Hoshino *et al.*, in *Proceedings of the 20th IAEA Fusion Energy Conference* (IAEA, Vienna, Vilamoura, Portugal, 2004) EX/4–6Rb.

[29] Y. Nagashima, K. Shinohara, K. Hoshino *et al.*, Plasma Phys. and Control. Fusion **46**, A381 (2004).

[30] K. Itoh, K. Hallatschek and S.-I. Itoh, Plasma Phys. and Control. Fusion **47**, 451 (2005).

[31] T. Ido, Y. Miura, K. Kamiya *et al.*, Plasma Phys. Control. Fusion **48**, S41 (2006).

[32] A. Kendl and B. Scott, Phys. Plasmas **13**, 012504 (2006).

[33] A. Fujisawa, H. Iguchi, T. Minami *et al.*, Phys. Rev. Lett. **82**, 2669 (1999).

[34] S. Okamura, T. Minami, T. Akiyama *et al.*, Nucl. Fusion **45**, 863 (2005).

[35] T. Oishii, S. Kado, M. Yoshinuma *et al.*, Nucl. Fusion **46**, 317 (2006).

[36] K. Nagaoka, M. Osakabe, M. Nishiura *et al.*, in *Proceedings of the 31th EPS Conference on Plasma Phys.* (EPS, London, UK, 2004) Vol. **28G**, P–5, 110.

[37] S. P. Hirshman, W. van RIJ and P. Merkel, Comput. Phys. Commun. **43**, 143 (1986).

[38] N. Kasuya and K. Itoh, Phys. Rev. Lett. **94**, 195002 (2005).